



Check for updates

RESEARCH ARTICLE

Rheological Modulation via Rigid-Flexible Polymer Network Engineering for High-Precision Photovoltaic Electrode Printing

¹School of Advanced Materials, Peking University Shenzhen Graduate School, Peking University, Shenzhen, China | ²Tsinghua-Berkeley Shenzhen Institute & Tsinghua Shenzhen International Graduate School, Tsinghua University, Shenzhen, China | ³Key Laboratory of Photochemistry, Chinese Academy of Sciences, Institute of Chemistry, Beijing, China

Correspondence: Luyi Yang (yangly@pkusz.edu.cn) | Yuan Lin (linyuan@iccas.ac.cn) | Feng Pan (panfeng@pkusz.edu.cn)

Received: 3 June 2025 | Revised: 20 July 2025 | Accepted: 28 July 2025

Funding: Soft Science Research Project of Guangdong Province, Grant/Award Number: 2017B030301013; Guangdong Innovative Team Program, Grant/

Award Number: 2013N080

Keywords: fine line screen-printing | organic carrier | rheological property | silver paste | solar cells

ABSTRACT

Screen printing remains vital for printed electronics due to its precision and substrate adaptability. In applications such as high-speed precision printing for silicon solar cell, the rheological properties of silver pastes are increasingly demanding. Conventional silver paste formulations suffer from insufficient shear stability and sluggish dynamic bond reorganization kinetics in polymer networks, resulting in severely degraded electrode printability. To overcome this limitation, we propose a rigid-flexible polymer synergy strategy designed to simultaneously enhance structural stability and dynamic self-healing capacity within the polymer network. Specifically, we employ a styrene-maleic anhydride (SMA) copolymer as a rheology modifier. We leverage the synergistic effects of reversible hydrogen bonds in flexible chains and steric hindrance by rigid segments. This synergy enhances high-speed printing precision. Furthermore, electrodes fabricated using this approach demonstrate a markedly improved aspect ratio while reducing silver consumption. The resulting sintered grid lines exhibit a densified cross-section morphology with lower porosity, leading to a reduced series resistance and enhanced power conversion efficiency. Collectively, these improvements enable photovoltaic performance on par with that of state-of-the-art commercial cells. This work offers a strategy for printable electrode optimization and reveals principles for designing polymer networks with tunable-rheology, paving the way for next-generation photovoltaic and electronic materials.

1 | Introduction

Screen printing has emerged as a critical manufacturing process for metallized electrodes in electronic devices, driven by its high precision, cost efficiency, and substrate compatibility [1]. The expanding applications of electronic pastes in information electronics demand enhanced printability and printing resolution. For instance, flatbed screen printing remains dominant in silicon solar cell metallization due to its optimized process economics and decades of industrial refinements in pattern fidelity. As the photovoltaic industry progresses in cost reduction and

efficiency enhancement, technological innovation remains critical. Developing high-aspect-ratio fine-line grid electrodes through optimized screen-printing processes is a strategically validated pathway [2–4]. Screen printing's defining feature is its adaptability to diverse substrates [5], enabling adjustable paste formulations to meet evolving needs. Significant progress has been achieved in minimizing electrode width and improving aspect ratio over the past decade [2, 6–8]. Currently, manufacturers are capable of ultra-fine grid lines with 10 μ m width printed at 500 mm/s speeds. However, narrowed screen apertures may cause electrode irregularities (e.g., fractures) after printing,

© 2025 Wiley-VCH GmbH.

reducing photovoltaic conversion efficiency. This requires optimizing paste rheology to match fine-feature patterns [9-11]. The printability of silver paste is determined by its rheological properties, particularly yield stress, shear-thinning behavior, and thixotropic recovery [12-15]. Typical formulations contain silver powders (up to 91 wt%), glass frits, and an organic carrier (containing thixotropic agents, solvents, thickeners, and others), synergistically controlling printing performance [16-18]. The organic carrier serves as the dispersion medium for inorganic powders, governing the paste's rheology and final electrode morphology and aspect ratio after printing and sintering [16, 19]. During high-shear printing, the carrier must exhibit optimal shear-thinning, thixotropic recovery, and structural regeneration [20-22]. Additionally, its volatilization and thermal decomposition dynamics critically affect sintered electrode resistivity [23-25].

Therefore, analyzing how silver paste composition affects electrode performance requires rheological characterization as a critical methodology. This approach allows precise quantification of mechanical responses in complex fluid systems under varying shear stress gradients or strain rate conditions [26]. For instance, the three-interval thixotropy test (3ITT) simulates practical screen-printing dynamics [27]. During printing, rotor-induced abrupt high-shear forces replicate blade scraping conditions, while the recovery phase mimics post-printing paste relaxation. Controlled frequency sweeps in oscillatory measurements systematically analyze the linear viscoelastic regime and modulus evolution in silver pastes [28, 29]. Wu et al. investigated the correlation between electrode gridline aspect ratio and PV cell conversion efficiency [30]. Tepner et al. established quantitative links between silver paste rheology and postprinting electrode morphology via parametric studies of printing velocity and wall-slip phenomena [6]. Durairaj et al. demonstrated that wall-slip effects mitigate electrode finger discontinuities, enabling further gridline width reduction while maintaining process robustness [31]. Qin et al. quantified organic carrier effects on front-side silver paste rheology through steady-state flow, 3ITT, and oscillatory experiments, with particle interaction strength characterized via yield stress analysis [32, 33].

Recent advances in silver paste printing have focused on optimizing organic carrier rheology and uncovering the compositional factors that govern print fidelity. For example, by adding a nonmiscible fluid, Zhao et al. achieved gridlines with H/W = 0.42, but the method relied on finely tuned particle and interfacial properties [34]. Tian et al. achieved an H/W ratio of 0.4505 through optimized solvent, binder, and coupling agent combinations [35]. Mao et al. developed a mixed-solvent strategy and used the Herschel-Bulkley model to identify carrier parameters conducive to high-aspect-ratio, high-fidelity printing [36]. Further, Tian et al. showed that adding 5 wt% PMSO and 4 wt% ED 120 lowered viscosity and improved recovery, yielding uniform gridlines with H/W = 0.4037 [37]. In parallel, Tepner et al. identified stable stencil permeability under low shear as a key challenge [2], while Kuzina et al. showed that organic gel architectures allow precise tuning of properties through composition control [38]. Together, these studies suggest strategies for balancing shear efficiency with network self-healing.

Although prior studies have connected formulation parameters to rheology and printing performance, understanding of how polymer structures and functional groups control mesoscale rheological behavior remains limited. As key components of the organic carrier, thixotropic agents and thickeners establish a dynamic reversible 3D gel network through hydrogen bonding, hydrophobic interactions, or dynamic covalent bonds. The shearstable polymer network in organic carriers plays a crucial role in governing the rheology of silver paste. It enables precise pattern replication during high-speed screen printing by supporting controlled viscosity recovery and dynamic bond reconfiguration. This study enhances polymer network structural stability and self-healing dynamics through functionally designed polymeric additives like styrene-maleic anhydride (SMA) copolymer, synergistically controlling gel network evolution. Notably, dynamic self-healing networks enable polymer chains to quickly reorganize after high shear during screen printing. This ensures fast structural recovery and stable viscosity for smooth mesh penetration. In parallel, rigid-flexible synergy maintains flowability under shear while preserving structural integrity. Together, these mechanisms significantly improve printing accuracy and pattern fidelity. Moreover, in situ Fourier-transform infrared (FTIR) spectroscopy and dynamic rheological analysis reveal how additives regulate viscoelastic responses in organic carriers. This is achieved through the synergistic effect of hydrogen bonding and steric hindrance, establishing a structure-property correlation between rheology and printability. The optimized silver paste exhibits enhanced thixotropy, rapid recovery, and improved print fidelity, achieving gridlines with an increased aspect ratio of 0.476 postsintering.

2 | Results and Discussion

2.1 | The Design and Selection of Additives

Advancing screen-printing demands precise rheological control of silver pastes, where tailored organic carriers enable uniform silver dispersion, reduced material usage, and improved power conversion efficiency (PCE). As shown in Figure 1, polyamide wax (thixotropic agent) and ethyl cellulose (thickener) are dispersed in alcohol esters using high-energy nanodispersion, forming a 3D gel network through molecular chain entanglement, hydrogen bonds, and van der Waals forces. This structure provides strong rheological and mechanical properties. However, it struggles to balance structural stability and rapid thixotropic recovery during high-speed, high-resolution printing, limiting precision-efficiency trade-offs. The key challenge is to optimize the gel network. This means integrating polar reactive groups to foster dynamic hydrogen-bonded networks, alongside rigid aromatic moieties that create steric confinement. Together, these elements boost both rheological properties and printability. Among conventional functionalized compounds, the styrene (ST) segment enhances hydrophobic compatibility with nonpolar systems via its rigid benzene rings. Maleic anhydride (MA) groups, with their high dipole moment ($\mu = 3.2$ D), forms dynamic networks through hydrogen bonding, enabling selfhealing and mechanical strength. The SMA copolymer, with the repeating unit -[CH₂CH (C₆H₅)-C₄H₂O₃]-_n, integrates the steric stabilizers of ST and the polar dynamic bonding capability of

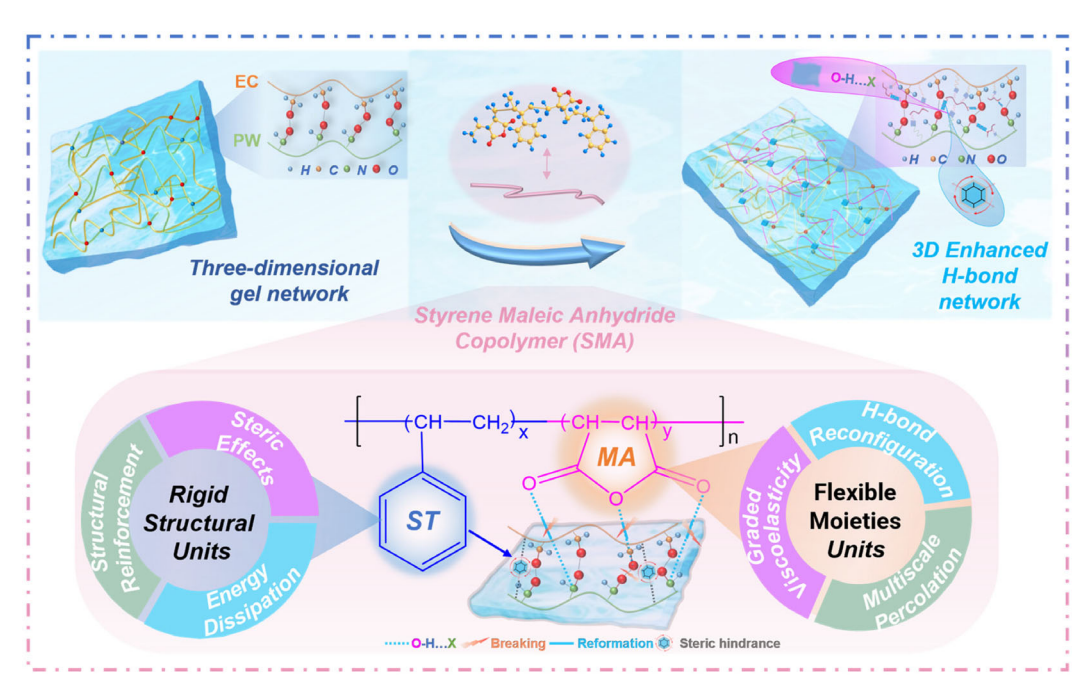


FIGURE 1 | Formation mechanism of 3D gel networks in silver paste carriers via SMA additive-mediated multifunctional interactions, with molecular architecture illustrating rigid-flexible group synergy for dynamic reinforcement.

MA, thereby emerging as a unique candidate for rheological modulation.

Building upon this model, this study established a structure-function cooperative design strategy for organic carrier systems using EC as the thickener and PW as the thixotropic agent. To systematically investigate the rheological mechanisms of the EC-PW composite system, organic carriers with varying PW/EC ratios

(detailed compositions in Table S1) were prepared and analyzed through dynamic oscillatory and steady-state rotational rheometry (results shown in Figure S1). These findings confirmed their critical roles in the organogel network, guiding precise ratio optimization. Figure 2a details the synergistic rheological interplay between yield stress and thixotropy across different PW/EC weight ratios. Under the optimized EC:PW ratio (O-2, 3.5:5.0 wt%), the system achieved peak print-stability metrics with thixotropic

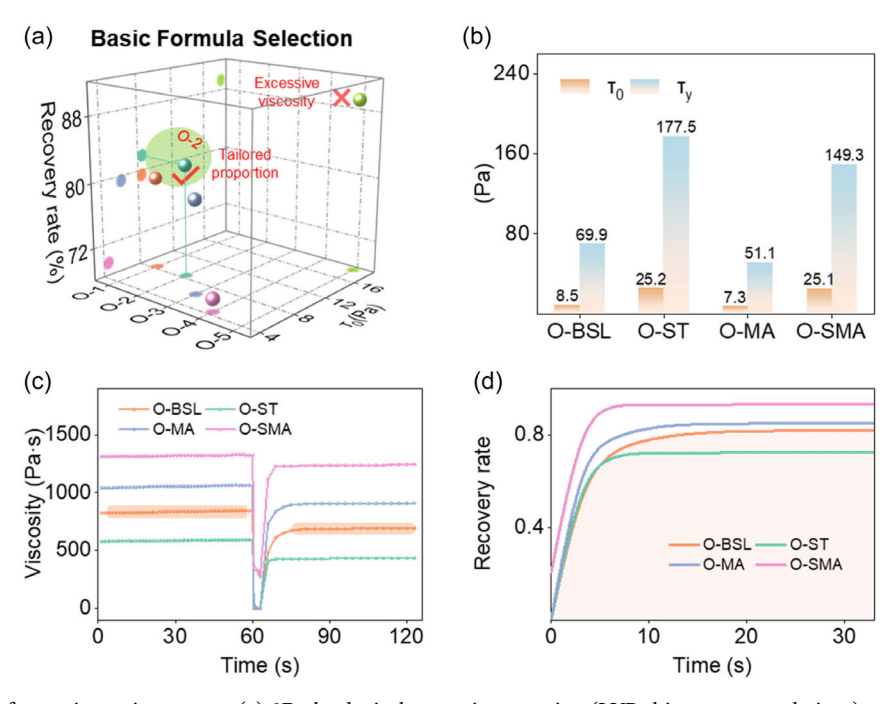


FIGURE 2 I Design of organic carrier system. (a) 3D rheological synergies mapping (LVR-thixotropy correlations) across PW:EC formulations. (b) The relationship between G' and G'' and shear stress obtained by oscillation amplitude sweep tests for organic carrier with additives featuring distinct functional groups. (c) Viscosity and (d) recovery rate during a three-step simulation of the screen-printing of organic carrier with additives featuring distinct functional groups. The shaded region denotes the experimental results obtained in the absence of additives.

recovery rate of 81.85% (via 3ITT protocol) and the linear visco-elastic region (LVR) ranges τ_0 of 8.49 Pa. In addition, three alcohol ester solvents (Table S2) with distinct surface tensions and boiling points were selected. TGA and volatilization profiles (Figure S2) confirmed their gradient evaporation capability. Through optimized surface tension-boiling point synergy, wettability tests on silicon wafers were conducted based on the organic solvent composition outlined in Table S3. The results reveal that the BCA: EPH:DBE = 6:3:1 ratio demonstrated superior wettability on silicon wafers with controlled gradient volatilization, as validated in Figure S3.

Further building on this foundation, this study systematically evaluated the rheological modulation effects of MA (flexible group), ST (rigid group), and their alternating copolymer SMA (rigid-flexible group) on the organic carrier (formulations detailed in Table S4). As shown in Figure 2b-d, flexible group (MA) system enhanced thixotropy via dynamic hydrogen bonding but reduced yield stress, while rigid groups (ST) improved yield stress at the expense of thixotropy. The rigid-flexible group (SMA) copolymer demonstrated synergistic effects. Further, by adjusting the St/MA molar ratios, the influence of functional group proportions on rheological performance was systematically investigated (Figure S4). Experimental results revealed that higher PS content decreased thixotropy due to steric hindrance impeding hydrogen bond reconstruction. Consequently, SMA-150 was prioritized as the additive to synergistically regulate the rheological properties of the organic carrier. Furthermore, FTIR (Figure S5a) and NMR (Figure S5b) confirmed the alternating copolymer structure, while TGA/DTG (Figure S5c) validated SMA-150's thermal stability (low-temperature volatilization, zero residue), effectively suppressing electrode porosity.

Furthermore, the compatibility and wettability effects of SMA on the organic carrier were evaluated (Figure S6). Solubility tests confirmed stable dissolution and compatibility of SMA in organic solvents. Dynamic contact angle measurements on silicon substrates revealed concentration-dependent wetting behavior. Lower SMA concentrations initially increased hydrophobicity, while higher concentrations enhanced wettability via hydrogen bonding. Optimal SMA content balanced wettability improvement with minimized over-spreading risks. On silver substrates, increasing additive concentrations reduced contact angles, indicating improved wetting behavior. Enhanced wettability promoted colloidally stable suspensions, suppressing sedimentation and agglomeration.

2.2 | Organic Carrier Test

After weighing the thixotropic agents, thickeners, additives, and organic solvents in specific proportions, the mixture was processed in a nanogrinding machine to form homogeneous organic carriers. Based on the additive composition ratios, the carriers were designated as O-SMA-X (additive concentration: 0.0–0.9 wt%, see Table S5).

Hydrogen bonds act as crosslinks in the organic carrier's 3D network, critically governing mechanical stability through noncovalent interactions. To investigate the mechanistic effects of additive incorporation on the network structure of organic

carrier, samples were analyzed via FTIR spectroscopy. Significantly, the O-H/N-H stretching vibrations within the 3300-3600 cm⁻¹ range are characteristic of hydrogen-bonding interactions. As shown in Figure 3a, the introduction of additives induced redshifted FTIR peaks with peak broadening and intensified absorbance. These changes confirm strengthened hydrogen bond and/or increased hydrogen-bond density. To correlate these structural modifications with macroscopic rheological behavior, rheological tests were conducted on the organic carriers. Figure 3b shows the viscosity profiles of organic carriers with varying additive concentrations under different shear rates. At 0.1 s⁻¹, the viscosity increased monotonically with additive loading, indicating enhanced network cohesion. At higher shear rates (1-10 s⁻¹), the viscosity exhibited a nonmonotonic trend, suggesting shear-thinning behavior critically modulated by additive concentration. This can be attributed to additives promoting molecular entanglement, but excessive additive loading introduces weak interactions that enable shear-activated molecular slippage, ultimately destabilizing the network. Therefore, optimizing additive concentration is key to balance network integrity and shear-responsive restructuring, essential for printability-stability equilibrium.

In addition, as quantified in Figure S7, all four organic carriers with varying additive concentrations exhibit pronounced shearthinning behavior. This rheological response is critical for the demands of the screen-printing process. The 3ITT was performed on organic carriers with varying additive concentrations to evaluate structural recovery kinetics, as shown in Figure 3c. The organic carrier containing additives exhibited a high instantaneous recovery rate in the early stage, which is beneficial for reducing the width of the fingers. Conversely, a lower instantaneous recovery rate may lead to the horizontal spreading of the silver paste after printing, thereby increasing the width of the fingers. Notably, the 0.6 wt% SMA carrier exhibited higher viscosity, which might hinder the paste from passing through the screen during the screen-printing process. Moreover, oscillatory amplitude sweeps measured the elastic (G') and viscous (G'') moduli to assess the LVR, revealing additive concentration effects on the carrier's viscoelastic performance. Figure 3d shows the G'/G" profiles, LVR ranges τ_0 and τ_v values for organic carriers with different SMA concentrations. The LVR ranges align with static mechanical analyses, exhibiting an initial increase followed by a decrease. The extended LVR correlated with a 152% enhancement for the 0.3 wt% SMA system versus the additive-free counterpart, attributable to reinforced network integrity. The gel points (defined as G' = G'') for carriers exhibit a consistent trend across concentration gradients, respectively. These results, detailed in Figure S8, show that additives stabilize the internal network. However, an excessively high gel point may have hindered the silver paste from passing through mesh openings during screen printing. In conclusion, rheological tests on the organic carrier show that adding additives significantly modulates viscosity and thixotropy. This is attributed to the reinforcement of its internal network structure and enhanced intermolecular cohesion. Specially, thermogravimetric analysis (TGA) confirmed residual mass < 0.3 wt% at 580°C for all carriers (Figure S9), demonstrating complete thermal decomposition. This ensures carbon-free sintering and unimpaired electrical contact in final devices. Based on a comprehensive comparison of rheological properties and printability, an SMA content

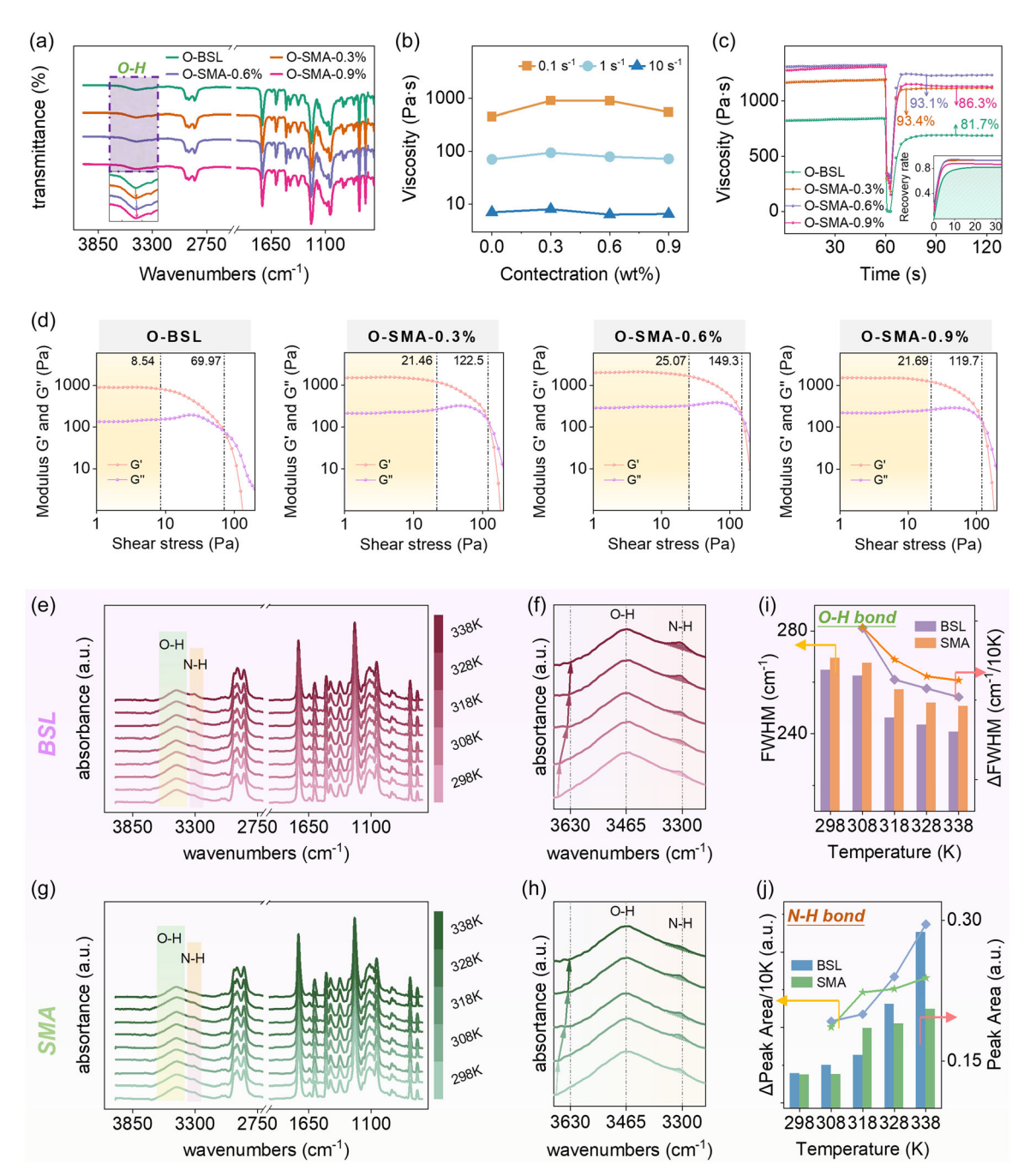


FIGURE 3 Characterization of the organic carrier properties modified by additive incorporation. (a) The infrared spectra and changes of hydrogenbond characteristic peaks of organic carriers. (b) Viscosity at different shear rates $(0.1, 1 \text{ and } 10 \text{ s}^{-1})$ for organic carriers. (c) The viscosity and recovery rate during a three-step simulation of the screen-printing of organic carriers. (d) The relationship between G' and G'' and shear stress obtained by oscillation amplitude sweep tests for organic carriers. (e,f) Variable-temperature infrared spectroscopy and hydrogen bond characteristic peak changes of the additive-free organic carrier. (g,h) Variable-temperature infrared spectroscopy and hydrogen bond characteristic peak changes of the organic carrier with 0.3 wt% additives. (i,j) Temperature-dependent evolution of FWHM and peak area for O–H/N–H hydrogen bonds, reflecting their differential thermal stability.

of 0.3 wt% is identified as optimal, exhibiting superior thixotropy, higher yield stress, and more suitable viscosity.

To further clarify the additive's function on the network architecture of organic carriers, this study employed in situ variable-temperature FTIR (298–338 K). This approach revealed how additives regulate the thermodynamics response of hydrogen-bond networks, with spectral evidence shown in Figure 3e–j. For the control group, the full width at half maximum

(FWHM) of the O-H stretching vibration peak at 3461 cm⁻¹ decreased sharply from 264.8 to 246.3 cm⁻¹ (6.98% reduction) at 318 K, indicating partial dissociation of the hydrogen-bonded network. Upon heating to 338 K, the integrated area of the N-H characteristic peak at 3307 cm⁻¹ surged from 0.0535 to 0.2732, confirming irreversible disintegration of the 3D network due to hydrogen bond rupture. In contrast, the system containing 0.3 wt% SMA additive maintained exceptional hydrogen-bond stability at 338 K, evidenced by the O-H peak FWHM decreased

only to $251.0\,\mathrm{cm}^{-1}$ (4.3% higher than control) and the change of N–H signal intensity remained negligible (0.1538). These results corroborate that the SMA copolymer constructs a stabilized dynamic gel network through the synergistic interplay between flexible (MA) and rigid (ST) moieties, providing molecular-level theoretical validation for the morphological stability of silver paste during high-temperature sintering.

2.3 | Effect on the Properties of Silver Paste

Unlike pure organic carrier systems, the rheology of silver pastes is dictated by polymer–particle interfacial dynamics, critically determining device performance. To dissect how additives modulate these interface-driven rheological responses during printing, SP-BSL and SP-SMA pastes were prepared by mixing glass frits and silver powders with organic carriers (without/with 0.3 wt% additives). The particle size and surface characteristics of the commercial glass frits and silver powders are shown in Figure S10.

Additionally, the flow behavior of these formulations was evaluated through rheological analysis. The results revealed a consistent viscosity increase in additive-modified pastes across all shear

rates compared to the control group (Figure 4a). This rheological shift aligns with the organic carrier's viscoelastic response, demonstrating strengthened internal network stability and improved particle cohesion. In parallel, shear-thinning behavior was distinctly observed in paste samples under variable shear rates from 0 to 120 s⁻¹ (Figure S11). To replicate actual screen-printing dynamics, the 3ITT were performed on the pastes (Figure 4b), applying a high-shear stress of 500 Pa in Stage 2 to emulate blade-passing conditions. Figure S12 shows the recovery rates during Stage 3 (low-shear restoration) for the silver paste. The results show that SP-SMA achieved 76.6% recovery within 30 s, outperforming the additive-free formulation. This highlights the additive's role in enabling partial pseudoplasticity (rapid postshear viscosity rebound). The paste's pseudoplasticity led to a swift increase in viscosity immediately after printing, thereby preventing further spreading and enhancing the aspect ratio of the printed lines. Although SP-BSL showed rapid initial recovery, excessive speed caused screen-paste adhesion and surface roughness during separation. Meanwhile, the oscillatory stress sweep test of the silver paste is a critical evaluation of its structural stability and viscoelasticity. As shown in Figure 4c,d, SP-BSL and SP-SMA exhibit LVR values of 131.9 and 143.5 Pa, respectively, demonstrating that additive incorporation broadens the LVR range by 8.8% while concurrently enhancing shear stability.

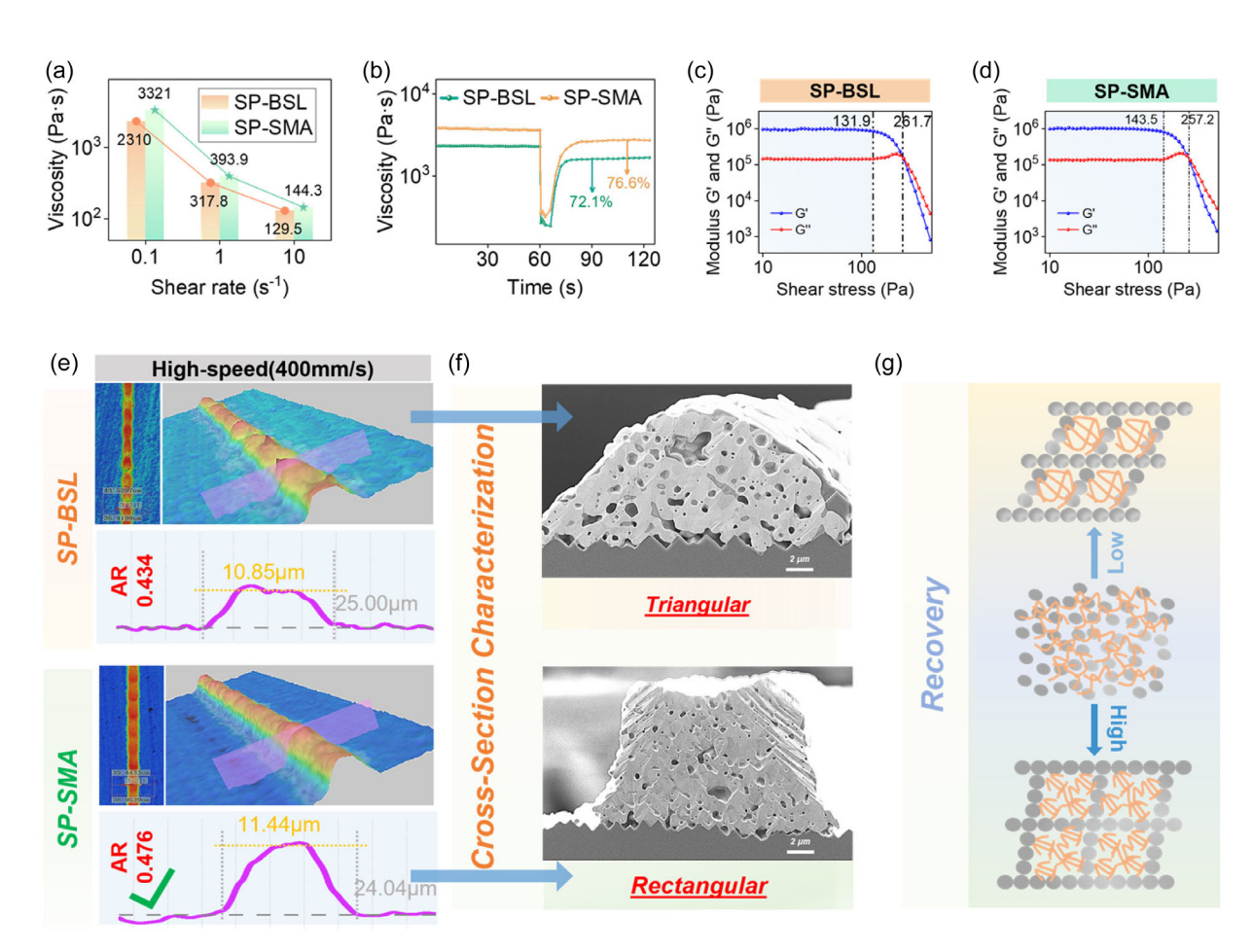


FIGURE 4 | Characterization of silver paste with the organic carrier properties modified by additive incorporation. (a) Viscosity of different shear rate $(0.1, 1, \text{ and } 10 \text{ s}^{-1})$ for silver pastes. (b) The viscosity during a three-step simulation of the screen-printing of silver pastes. (c,d) The relationship between G' and G" and shear stress obtained by oscillation amplitude sweep tests for silver pastes. (e) 3D microscopic image and (f) cross-sections of the electrode surfaces after screen printing for silver pastes. (g) Schematic illustration of the microstructural evolution of silver pastes with/without additives during the recovery process of screen printing.

Notably, the paste with higher yield stress exhibited superior shape retention under high stress. This mechanical robustness prevents line collapse during screen withdrawal, ensuring high aspect ratio for printed patterns. To verify printability, the fineness (particle size distribution) of the pastes was characterized (Figure S13). All formulations achieved particle sizes $< 5\,\mu m$, meeting the threshold for unimpeded mesh penetration, which can achieve normal printing.

To bridge the rheological properties with practical application outcomes, we systematically investigated the printing fidelity of silver pastes. Figure 4e,f present the 3D morphological analysis and cross-sections of screen-printed electrodes fabricated with different silver pastes with/without additives under high-speed printing conditions. Due to divergent rheological properties, the printed electrodes exhibited distinct line geometries and surface topographies, with all formulations showing ink spreading (electrode widths $> 15 \mu m$). The results showed that the additivefree paste (SP-BSL) demonstrated significant post-printing collapse and uneven height profiles, yielding a width of 25.00 μm, height of 10.85 µm, and aspect ratio of 0.434, accompanied by pronounced surface roughness. This instability was attributed to its lower viscosity and network stability (a smaller τ_{ν}), which led to irreversible structural breakdown under high shear stress. In contrast, electrodes printed with the additive-modified paste (SP-SMA) exhibited markedly improved morphological integrity and smoother surface topography. Its elevated viscosity and extended LVR enhanced structural resilience, enabling uniform paste deposition with reduced spreading (width = $24.04 \mu m$, height = $11.44 \,\mu\text{m}$, and aspect ratio = 0.476). These results confirm that additive incorporation optimizes the balance between shear-thinning flowability and structural recovery, which is critical for high-resolution printing behavior. As shown in Figure 4g, during silver paste screen printing, high shear in the printing stage generates shear stress. This induces partial disintegration of the flocculated network, and the resulting shear-thinning behavior enables pseudoplastic flow through mesh openings. Postprinting recovery after stress removal resulted in >70% network restoration within seconds via reformation of dynamic bonds (hydrogen bonds and van der Waals forces) and recoiling of flexible polymer chains. Notably, the optimized organic carrier exhibited enhanced hydrogen-bonding networks with dynamic self-healing capacity and robust stability. These characteristics amplify intermolecular interactions during recovery, thereby achieving concurrent improvements in network reconstruction efficiency and line fidelity. To probe additive concentration effects, an additional formulation (SP-SMA-0.6 wt%) was prepared using the organic carrier with elevated additive concentration (O-SMA-0.6 wt%). As shown in Figure S14, this high-additive paste exhibited rheological properties aligned with its carrier's characteristics but demonstrated diminished printing performance compared to SP-SMA.

2.4 | Effect on Solar Cell Performance

To comprehensively assess the impact of additive incorporation on the electrical performance of screen-printed solar cells, silver pastes were screen-printed onto laser-cut commercial-grade monocrystalline silicon wafers $(35 \times 53 \text{ mm})$ and subjected to cofiring in an industrial belt furnace. Notably, as shown in

the analysis of Table S6, the use of wafers in this laser-cut size led to a decrease in light absorption area, altered carrier collection paths, and increased recombination due to laser-induced edge damage, resulting in a baseline efficiency of $\approx 14\%$. Multiple replicates were prepared for each formulation ensured statistical robustness All comparative experiments used samples cut from the same batch of wafers under strictly uniform cutting parameters and test conditions, thereby confirming that observed performance differences were solely attributable to paste characteristics. 3D morphological analysis of the electrode grids (Figure 5a) revealed that adding the additive significantly enhanced the regularity of the electrode morphology. The height, width, and aspect ratio all exhibited enhanced consistency with the trends observed in previous experiments. Besides, silver paste is one of the most expensive consumables in photovoltaic cell manufacturing, where precise control of postprinting wet weight critically impacts both device efficiency and production costs. As shown in Figure 5b, systematic testing result revealed that the additive-modified silver paste (Cell-SMA) exhibited a wet weight of 5.82 mg/p, compared to 7.12 mg/p for the baseline sample (Cell-BSL), with 10 replicates per sample to ensure precision and reliability of the data. This reduction stems from narrower printed line width (23.08 µm vs. 24.04 µm) and enhanced rheological stability, significantly lowering production costs.

As shown in Figure S15, to further evaluate the additive's impact on electrode electrical performance, screen-printed electrodes (350 mm length) were fabricated and characterized. Electrode resistance (R) were measured using a UNI-T UT620C Multimeter, with cross-sectional area measured by 3D microscopy. Contact resistance (R_c) at the silver-silicon interface was quantified using the transmission line model (TLM). As shown in Figure 5c and Table S7, the Cell-SMA exhibited superior performance compared to the additive-free counterpart. The line resistance decreased to $3.30\,\Omega$ (from $3.54\,\Omega$ for the control). Simultaneously, the R_c at the electrode-silicon interface was optimized to 1.033 m Ω , representing a 12.7% reduction. To elucidate the origin of electrical performance variations among sintered electrodes, scanning electron microscopy (SEM) was utilized to analyze the porosity of electrode surfaces. As shown in Figure 5d, the Cell-SMA exhibited a surface porosity of 1.028%, approximately 10.9% lower than that of the Cell-BSL. Notably, the Cell-SMA sample exhibited quasi-circular pore morphologies with a narrow size distribution of $0.4-0.8 \mu m$, while the control cell group demonstrated irregular pore geometries spanning a broader range of 0.5–1.1 μm. Concurrently, the Cell-SMA demonstrated a denser and more homogeneous microstructure, marked by fewer voids and enhanced interconnectivity of silver grains. These factors contributed positively to enhancing the conductivity of the printed electrodes.

To validate the commercial viability of the developed silver paste, a comparative assessment was conducted against a leading commercial silver paste (denoted as Commercial) using identical screen-printing and characterization protocols. To further evaluate their electrical performance, pulsed solar simulation and digital source meter measurement were performed. The I–V curves of the tests are detailed in Figure 5e. The analysis results indicate that compared to Commercial, Cell-SMA showed strong competitiveness in electrical performance indicators such as fill factor (FF) and series resistance ($R_{\rm s}$), and more detailed electrical

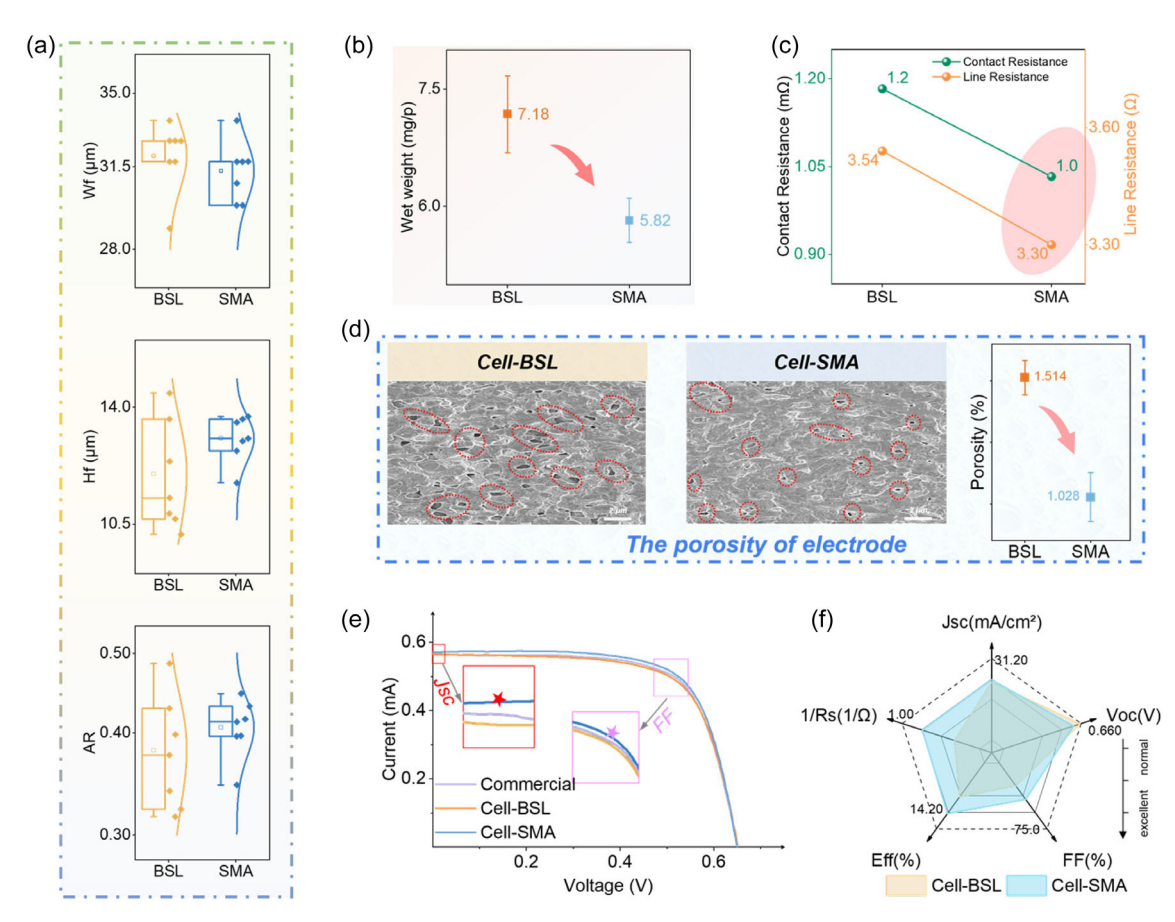


FIGURE 5 | Characterization of solar cells with/without additives. (a) Comparison of line dimensions and aspect ratio for cells. (b) Printing wet weight (mg/p) for cells. (c) Electrical performance parameters for cells. (d) The porosity of the electrode surfaces for cells. (e) I–V curves for cells prepared with different experimental and commercial pastes. (f) Radar chart of photovoltaic performance comparison for cells.

performance test data can be consulted in Table S8. Additionally, the radar chart comparing photovoltaic performance of cells with/without additives is shown in Figure 5f. Cell-SMA demonstrated superior electrical performance, achieving an FF of 69.99%, a R_s of 1.224 m Ω , and a PCE of 14.08%, all surpassing Cell-BSL. Detailed data comparisons are provided in Table S9. These improvements stem from the paste's optimized rheological properties, which enabled high-yield printing of electrodes with uniform grid lines and minimized shading area. To further assess the influence of additive concentration on solar cell performance, cells fabricated with the higher-additive-ratio silver paste (SP-SMA-0.6%, denoted as Cell-SMA-0.6%) were subjected to identical electrical characterization. As shown in Figure S16. Table S10 and S11, the resulting cells exhibited electrical performance trends consistent with the rheological and morphological characteristics of both the silver paste and its organic carrier.

In addition to electrical performance, the reliability of solar cells using the new silver paste is also worthy of attention. Given that both the organic carrier and SMA are completely volatilized during sintering, our analysis focuses on the regulatory role of SMA on the microstructure of the silver layer during this stage. Specifically, SMA facilitates the dispersion and densification of silver particles, reducing porous defects in the silver layer and thereby effectively inhibiting silver ion migration and electrical performance degradation under humid and hot conditions. Furthermore, prior to volatilization, the polar groups of SMA

enhance the interfacial wettability between silver particles and silicon wafers, which helps form more stable ohmic contacts. These analyses, based on the intrinsic structure-property relationships, provide theoretical support for the improved reliability of the new silver paste. Subsequent experiments will validate relevant reliability metrics to refine the conclusions.

3 | Conclusions

This study addresses the challenges of fine-line screen printing technology by strategically modifying organic carriers with SMA copolymers. The SMA leverages functional group interactions to construct a hybrid 3D network synergizing physical entanglement and dynamic hydrogen bonding. Importantly, this dynamic self-healing network enables rapid polymer chain reorganization after shear disruption, while the rigid-flexible synergy balances flowability and structural integrity during high-speed printing, fundamentally enhancing print precision. Rheological characterization revealed that the 0.3 wt% SMA-modified carrier exhibits an instantaneous thixotropic recovery rate of 93.4% and an extended LVR (LVR = 25.07 Pa). These synergistic properties enable precise paste control during high-speed printing. The resultant silver paste demonstrates enhanced thixotropy, optimal recovery rate, and stability. After the screen printing and sintering process, the wet weight of the electrode is reduced, the morphology of the metal grid lines is more regular, and the aspect

ratio reaches 0.476. In addition, the PCE, fill factor, and series resistance are all improved. These advancements achieved electrical performance rivaling state-of-the-art commercial products. This study reveals the synergistic role of organic carriers in rheological tuning. It highlights the fundamental significance of multiscale particle-polymer-solvent interactions, which are central to colloid and interface chemistry. The work provides theoretical guidance for high-precision screen printing and lays the groundwork for next-generation microgel-engineered systems in ultrafine line printed electronics.

Acknowledgements

The author is thankful for the support of the Soft Science Research Project of Guangdong Province (no. 2017B030301013), and Guangdong Innovative Team Program (no. 2013N080). The author is profoundly indebted to Dr. Rui Zhou for his seminal contributions to organic carrier development.

Conflicts of Interest

The authors declare no conflicts of interest.

Data Availability Statement

The data that support the findings of this study are available in the supplementary material of this article.

References

- 1. M. Bertolino, D. Battegazzore, R. Arrigo, et al., "Designing 3D Printable Polypropylene: Material and Process Optimisation through Rheology," *Additive Manufacturing* 40, (2021): 101944.
- 2. S. Tepner and A. Lorenz, "Printing Technologies for Silicon Solar Cell Metallization: A Comprehensive Review," *Prog Photovoltaics* 31, no. 6 (2023): 557–590.
- 3. K. A. Aal and N. Willenbacher, "Front Side Metallization of Silicon Solar Cells A High-Speed Video Imaging Analysis of the Screen Printing Process," *Solar Energy Materials & Solar Cells* 217, (2020): 110721.
- 4. C. Yuece, K. Okamoto, L. Karpowich, et al., "Non-Volatile Free Silver Paste Formulation for Front-Side Metallization of Silicon Solar Cells," *Solar Energy Materials & Solar Cells* 200, (2019): 110040.
- 5. M. Ali, L. Lin, S. Faisal, et al., "Optimisation of Screen Printing Process for Functional Printing," *Pigment & Resin Technology* 48, no. 5 (2019): 456–463.
- 6. S. Tepner, N. Wengenmeyr, M. Linse, et al., "The Link between Ag-Paste Rheology and Screen-Printed Solar Cell Metallization," *Advanced Materials Technologies* 5, no. 10 (2020): 2000654.
- 7. S. Tepner, L. Ney, M. Singler, et al., "A Model for Screen Utility to Predict the Future of Printed Solar Cell Metallization," *Scientific Reports* 11, no. 1 (2021): 4352.
- 8. S. Tepner, L. Ney, M. Linse, et al., "Screen Pattern Simulation for an Improved Front-Side Ag-Electrode Metallization of Si-Solar Cells," *Prog Photovoltaics* 28, no. 10 (2020): 1054–1062.
- 9. F. Hoeng, A. Denneulin, N. Reverdy-Bruas, et al., "Rheology of Cellulose Nanofibrils/Silver Nanowires Suspension for the Production of Transparent and Conductive Electrodes by Screen Printing," *Applied Surface Science* 394 (2017): 160–168.
- 10. D. Li, X. Liu, X. Chen, et al., "A Simple Strategy towards Highly Conductive Silver-Nanowire Inks for Screen-Printed Flexible

- Transparent Conductive Films and Wearable Energy-Storage Devices," *Advanced Materials Technologies* 4, no. 8 (2019): 1900196.
- 11. B. H. Teo, A. Khanna, V. Shanmugam, et al., "Development of Nanoparticle Copper Screen Printing Pastes for Silicon Heterojunction Solar Cells," *Solar Energy* 189 (2019): 179–185.
- 12. M. Pospischil, J. Specht, M. Koenig, et al., "Paste Rheology Correlating With Dispensed Finger Geometry," *IEEE Journal of Photovoltaics* 4, no. 1 (2014): 498–503.
- 13. A. Lorenz, A. Muenzer, M. Lehner, et al., High-Throughput Front and Rear Side Metallization of Silicon Solar Cells Using Rotary Screen Printing; Proceedings of the 7th International Conference on Crystalline Silicon Photovoltaics (SiliconPV), (Fraunhofer ISE, 2017), F 2017 Apr 03-05, 2017.
- 14. S. Thibert, J. Jourdan, B. Bechevet, et al., "Influence of Silver Paste Rheology and Screen Parameters on the Front Side Metallization of Silicon Solar Cell," *Materials Science in Semiconductor Processing* 27 (2014): 790–799.
- 15. M. Pospischil, K. Zengerle, J. Specht, et al., Investigations of Thick-Film-Paste Rheology for Dispensing Applications; Proceedings of the 1st International Conference on Crystalline Silicon Photovoltaics (SiliconPV), (2011), F 2011 Apr 17-20, 2011.
- 16. H.-W. Lin, C.-P. Chang, W.-H. Hwu, et al., "The Rheological Behaviors of Screen-Printing Pastes," *Journal of Materials Processing Technology* 197, no. 1–3 (2008): 284–291.
- 17. L. K. Q. Yan, S. K. Tam, K. Y. Fung et al., "Product Design: Formulation of a Screen-Printable Sintering-Type Conductive Paste," *AlChE Journal* 66, no. 8 (2020): 16272.
- 18. S. J. Jeon, S. M. Koo, and S. A. Hwang, "Optimization of Lead- and Cadmium-Free Front Contact Silver Paste Formulation to Achieve High Fill Factors for Industrial Screen-Printed Si Solar Cells," *Solar Energy Materials and Solar Cells* 93, no. 6-7 (2009): 1103–1109.
- 19. K. Inukai, Y. Takahashi, K. Ri, et al., "Rheological Analysis of Ceramic Pastes with Ethyl Cellulose for Screen-Printing," *Ceramics International* 41, no. 4 (2015): 5959–5966.
- 20. S. Thibert, J. Jourdan, B. Bechevet, et al., "Study of the High Throughput Flexographic Process for Silicon Solar Cell Metallisation," *Prog Photovoltaics* 24, no. 2 (2016): 240–252.
- 21. C. Xu and N. Willenbacher, "How Rheological Properties Affect Fine-Line Screen Printing of Pastes: A Combined Rheological and High-Speed Video Imaging Study," *Journal of Coatings Technology and Research* 15, no. 6 (2018): 1401–1412.
- 22. J. Zhang, Y. Cui, and H. Wang, "Optimization of Viscosity and Thixotropy for Organic Medium to Achieve High Photovoltaic Conversion Efficiency of Silicon Solar Cells," *Journal of Renewable and Sustainable Energy* 5, no. 2 (2013): 023117.
- 23. R. Li, H. Wang, Y. Tai, et al., "Influence of the Properties of Organic Media in Back-Side Silver Pastes on the Electrical Performance of Polycrystalline Silicon Solar Cells," *RSC Advances* 6, no. 49 (2016): 43732–43739.
- 24. R. Gan, J. Li, X. Cao, et al., "Mixed Solvents in Multilayer Ceramic Capacitors (MLCC) Electronic Paste and Their Effects on the Properties of Organic Vehicle," *Polymers* 14, no. 4 (2022): 685.
- 25. Y. Gao, J. Feng, F. Liu, et al., "Effects of Organic Vehicle on the Rheological and Screen-Printing Characteristics of Silver Paste for LTCC Thick Film Electrodes," *Materials* 15, no. 5 (2022): 1953.
- 26. C. Cui, T. Nie, B. Zhou, et al., "Preparation and Investigation of Graphene-Coated Lead-Free Glass Frit Based on Amino Dispersant for Improved Adhesion and Lower Temperature Point," *Diamond and Related Materials* 111, (2021): 108213.
- 27. M. Go, X. Qi, P. Matteini, et al., "High Resolution Screen-Printing of Carbon Black/Carbon Nanotube Composite for Stretchable and Wearable

Strain Sensor with Controllable Sensitivity," Sensors and Actuators. A, Physical 332, (2021): 113098.

- 28. J.-S. Jiang, J.-E. Liang, H.-L. Yi, et al., "Performances of Screen-Printing Silver Thick Films: Rheology, Morphology, Mechanical and Electronic Properties," *Materials Chemistry and Physics* 176 (2016): 96–103.
- 29. R. Durairaj, S. Ramesh, S. Mallik, et al., "Rheological Characterisation and Printing Performance of Sn/Ag/Cu Solder Pastes," *Materials Design* 30, no. 9 (2009): 3812–3818.
- 30. S. WU, J. ZHANG, Z. WANG, et al., "High-Aspect-Ratio Silver Grids of Solar Cells Prepared by Direct Writing," *Solar Energy Materials & Solar Cells* 259, (2023): 112452.
- 31. R. Durairaj, L. W. Man, N. Ekere, and N. etal, "The Effect of Wall-Slip Formation on the Rheological Behaviour of Lead-Free Solder Pastes," *Materials Design* 31, no. 3 (2010): 1056–1062.
- 32. J. Qin, S. Bai, W. Zhang, et al., "Effects of Organic Medium on Rheological Properties of Silver Pastes for Crystalline Silicon Solar Cells," *Circuit World* 42, no. 2 (2016): 77–83.
- 33. J. Qin, W. Zhang, Z. Liu, et al., "Effects of Polymer Binder on Rheological Properties of Silver Pastes for Screen Printing Front Electrode Films of Solar Cells," *International Journal of Modern Physics. B* 29, no. 10-11, (2015): 1540027.
- 34. S. Zhao, K. Hu, M. Huang, et al., "Optimization of Capillary Suspension Silver Pastes for Enhanced Metallization in Silicon Solar Cells: A Comparative Analysis of Screen-Printing and Pattern Transfer Printing," *Solar Energy* 277, (2024): 112746.
- 35. Y. Tian, C. Mao, X. Zhou, et al., "An Optimization Strategy for Improving the Aspect Ratio of Screen Printing Electronic Paste Based on Rheological Properties," *Colloid Surface A* 697, (2024): 134453.
- 36. C. Mao, Y. Tian, X. Zhou, et al., "Unification of Rheology of Thixotropic Yield Stress Fluids and Screen Printing Properties of Pastes," *Colloid Surface A* 682, (2024): 132982.
- 37. Y. Tian, C. Mao, Q. Li, et al., "How Do Organic Additives Affect the Properties of Electronic Pastes: A Combined Study of Rheology and Printability," *Journal of Materials Science in Electronics* 36, no. 4 (2025): 244.
- 38. M. A. Kuzina, D. D. Kartsev, A. Stratonovich, and V. etal, "Organogels versus Hydrogels: Advantages, Challenges, and Applications," *Advanced Functional Materials* 33, no. 27 (2023): 2301421.

Supporting Information

Additional supporting information can be found online in the Supporting Information section. Supporting Fig. S1 (a) Viscosity during a three-step simulation of the screen-printing of organic carriers. The shaded area indicates excessively high viscosity, which hinders paste penetration efficiency during screen printing. (b) The relationship between G' and G" and shear stress obtained by oscillation amplitude sweep tests. The region above the shaded threshold corresponds to excessive yield stress (>90 Pa), leading to inconsistent paste transfer through the screen. Supporting Fig. S2 (a) Volatility profiles and the (b) TGA curves of organic solvents (EPH, DBE, BCA). Supporting Fig. S3 (a) Contact angle and (b) timevarying contact angles of organic solvents on silicon wafers. Supporting Fig. S4 (a) Viscosity and (b) recovery rate during a three-step screenprinting simulation for organic carriers with St/MA molar ratios. Supporting Fig. S5 (a) FTIR spectrum of SMA copolymer. (b) 13CNMR and 1HNMR spectra of SMA copolymer. (c) TGA and DTG curves of SMA polymer. Supporting Fig. S6 (a) The solubility of the organic solvents with varying concentrations of additives. (b-c) The contact angle of different additive solutions on silicon substrate and silver powders substrates. Supporting Fig. S7 Shear viscosity of organic carriers with different additive concentrations (0.0-0.9 wt%) under variable shear rates (0-120 s-1). Supporting Fig. S8 Oscillatory amplitude sweeps results (shear stress vs. strain) for organic carriers with additive concentrations (0.0-0.9 wt%). Supporting Fig. S9 TGA curves of organic carriers with additive concentrations (0.0-0.9 wt%). Supporting Fig. S10 Particle size distribution and SEM morphology of (a) commercial glass frits. (b) silver powders. Supporting Fig. S11 Shear viscosity of silver pastes with additive concentrations (0.0 wt%, 0.3 wt%) under variable shear rates (0-120 s-1). Supporting Fig. S12 Recovery rate during threestep screen-printing simulation for silver pastes with additive concentrations (0.0 wt%, 0.3 wt%). Supporting Fig. S13 Fineness (particle size <5 um) of silver pastes with additive concentrations (0.0 wt%, 0.3 wt%) measured via scraper fineness gauge. Supporting Fig. S14 Rheological and printing performance of SP-SMA-0.6 wt% paste. (a) Viscosity at γ . = 0.1, 1 and 10 s-1. (b) Shear-thinning behavior (0-120 s-1). (c) Viscosity during three-step printing simulation. (d) Thixotropic recovery rate. (e) G'-G" crossover from oscillatory amplitude sweeps. (f) 3D morphology and cross-sections under varied printing speeds. Supporting Fig. S15 Electrical characterization methodology. (a) transmission line model (TLM) for contact resistance (Rc). (b) Line resistance (Rl) measurement schematic. Supporting Table S1 Composition of organic carriers with varying PW/EC mass ratios. Supporting Table S2 Physicochemical properties of organic solvents. Supporting Table S3 Composition of organic solvents in mixed systems Supporting Table S4 Composition of organic carriers with styrene-maleic anhydride (St/MA) molar ratios (SMA-125: 3:1; SMA-130: 2:1; SMA-150: 1:1) Supporting Table S5 Composition of organic carriers with additives concentrations (0.0-0.9 wt%). Supporting Table S6 Comparison of silicon wafer performance parameters before and after laser cutting. Supporting Table S7 Resistive properties of Cell-BSL and Cell-SMA. Supporting Table S8 Photovoltaic performance of Commercial, Cell-BSL, and Cell-SMA under standard test conditions. Supporting Table S9 Photovoltaic performance of Cell-BSL and C ell-SMA(best). Supporting Table S10 Resistive properties of Cell-SMA-0.6 wt%. Supporting Table S11 Photovoltaic parameters of Cell-SMA-0.6 wt%.